

## The Long-Term Flux of the Solar Wind Suprathermal Ions That Precipitate on the Lunar Surface

Q. Nénon<sup>1</sup> , J. M. Raines<sup>2</sup> , and A. R. Poppe<sup>3</sup> 

<sup>1</sup>IRAP, UPS-CNRS-CNES, Toulouse, France, <sup>2</sup>Department of Climate and Space Sciences Engineering, University of Michigan, Ann Arbor, MI, USA, <sup>3</sup>Space Sciences Laboratory, University of California, Berkeley, Berkeley, CA, USA

### Key Points:

- Wind-STICS constrains the long-term flux of the suprathermal solar wind ions that weather the lunar surface
- The 17-year-averaged energy spectra of protons, helium ions, and oxygen ions are in agreement with an 11-month estimate published in 2001
- Lunar Permanently Shadowed Regions are weathered by the same flux of >15 keV/nucleon ions as anywhere else on the lunar surface

### Supporting Information:

Supporting Information may be found in the online version of this article.

### Correspondence to:

Q. Nénon,  
q.nenon@gmail.com

### Citation:

Nénon, Q., Raines, J. M., & Poppe, A. R. (2023). The long-term flux of the solar wind suprathermal ions that precipitate on the lunar surface. *Journal of Geophysical Research: Planets*, 128, e2023JE007958. <https://doi.org/10.1029/2023JE007958>

Received 15 JUN 2023  
Accepted 20 OCT 2023

**Abstract** Solar wind ions weather the optical, physical, and chemical properties of the lunar surface. While the solar wind ion number density is dominated by the thermal population, the study of suprathermal ions is important to understand weathering effects that may develop at depth larger than the penetration depth of the bulk solar wind. Possible manifestations of suprathermal ion weathering include the creation of thick amorphous rims, contamination of isotopic ratios at depth, and alteration of the optical reflectance at infrared wavelengths. Furthermore, while the thermal population forms a beam parallel to the ecliptic plane, suprathermal ions may have a large northward or southward velocity component and can therefore directly access and weather the lunar polar regions, including the interiors of the Permanently Shadowed Regions (PSRs). In this article, we constrain the long-term properties of the solar wind suprathermal ions using 17 years of observations by the SupraThermal Ion Composition Spectrometer onboard the Wind spacecraft (Wind-STICS). We find that the 17-year omnidirectional energy spectra of protons, helium ions, and oxygen ions observed by Wind-STICS are in excellent agreement with the 11-month estimates published by Mewaldt et al. (2001, <https://doi.org/10.1063/1.1433995>) and Mewaldt et al. (2007, [https://doi.org/10.1007/978-0-387-74184-0\\_32](https://doi.org/10.1007/978-0-387-74184-0_32)). This agreement validates the conclusions of Nénon and Poppe (2020, <https://doi.org/10.3847/PSJ/abbe0c>) who proposed that suprathermal ions heavier than helium may increase the rate of amorphous rim formation in lunar samples by 50%. Furthermore, the Wind-STICS observations of out-of-ecliptic ions reveal that the lunar PSRs are weathered by the same flux of >15 keV/nucleon as anywhere else on the lunar surface.

**Plain Language Summary** The lunar surface is directly exposed to space and constantly bombarded by positively charged particles known as “ions.” These particles in turn modify the optical, physical, and chemical properties of the planetary surface. In this article, we use 17 years of ion observations by the Wind spacecraft to constrain the long-term-averaged characteristics of the ions flowing in the solar wind with a velocity much greater than the solar wind group speed. Owing to their greater velocity, these fast ions can modify the surface at larger depth than typical solar wind particles. We find that the long-term 17-year flux of fast ions observed by Wind is consistent with an 11-month estimate previously published in 2001. We also find that the fluxes of ions flowing in and out of the ecliptic plane, where most planets orbit, become similar above a minimum ion velocity. This finding reveals that the interiors of the lunar polar craters, which are not exposed to the typical solar wind, are in fact altered by at least these out-of-ecliptic ions. The presented characterization of precipitating ions is a first step toward understanding the alteration of polar craters by space plasma ions, including the sources and sinks of water ice.

## 1. Introduction

In the solar system, the surfaces of airless bodies unprotected by thick atmosphere or large-scale magnetic field are directly bombarded and weathered by the positively charged ions of the solar wind: H<sup>+</sup>, He<sup>++</sup>, C<sup>4-6+</sup>, N<sup>5-7+</sup>, O<sup>6-8+</sup>, Ne<sup>7-9+</sup>, O<sup>7-10+</sup>, Si<sup>6-12+</sup>, S<sup>6-11+</sup>, Fe<sup>6-14+</sup> (von Steiger et al., 2000). Solar wind ions can be organized into three families based on their kinetic energy.

First, “thermal” ions have a kinetic energy close to that imposed by the solar wind bulk speed of 400 km/s to 800 km/s, corresponding to ion kinetic energies of 0.8 keV/nucleon to 3.2 keV/nucleon. Ions with a kinetic energy between around 2–3 keV/nucleon and 100 keV/nucleon are usually known as “suprathermal” ions. The exact definition of the low energy boundary of the suprathermal ion population can depend on the thermal bulk speed. For instance, Gruesbeck et al. (2015) set the lower energy limit of suprathermal ions at twice the solar wind speed. Suprathermal ions may always be present as the suprathermal tail of the thermal population and their

© 2023. The Authors.

This is an open access article under the terms of the [Creative Commons Attribution License](https://creativecommons.org/licenses/by/4.0/), which permits use, distribution and reproduction in any medium, provided the original work is properly cited.

fluxes can increase during solar wind events (Mewaldt et al., 2001, 2007). Finally, ions with a kinetic energy greater than 100 keV/nucleon are labeled as “energetic” ions.

When the thermal, suprathermal, and energetic ions impact an airless body surface, they alter the optical, physical, and chemical properties of the irradiated matter via an ensemble of processes referred to as “ion weathering.” In the following paragraphs, we introduce the main ion weathering mechanisms proposed to occur on the lunar surface (Jordan, 2022; Pieters & Noble, 2016) with the intent to identify the processes to which suprathermal ions can contribute, thereby motivating the study of this ion population.

Impacting ion transfers its energy to target material atoms via elastic and non-elastic collisions. These collisions can displace atoms out of their crystal lattice and generate two main ion weathering mechanisms. The first one is ion sputtering, which occurs when a knocked atom leaves the surface with a kinetic energy greater than the surface binding energy (e.g., Schaible et al., 2017). However, Nénon and Poppe (2020) have shown that suprathermal ions contribute only a minor addition to ion sputtering (see Figure 2b of Nénon and Poppe (2020)).

The second effect of ion-induced atomic displacements is the creation of amorphous rims on top of lunar and asteroid regolith grains (e.g., Keller & Zhang, 2015; Keller et al., 2021). Keller et al. (2021) have shown that the rim thickness onto lunar regolith grains increases with exposure time to ion irradiation until a depth plateau is reached. Still, some amorphous rims are much thicker than the penetration depth of thermal ions, so Poppe et al. (2018) proposed that the thick rims could be an effect of deeply-penetrating suprathermal ions.

The impacting ion can also deposit an exogenous atom in the planetary surface material. Evidence for contamination by suprathermal ions at depth, known as the “SEP component” among cosmochemists, has long been debated and has finally been dismissed by the Genesis mission (Wieler, 2016). Contamination by suprathermal ions may therefore be too small to significantly alter the material composition. However, most analysis focus on rare gas because they do not react with the planetary matter, while the most abundant solar wind species are hydrogen, helium, carbon, and oxygen. The contamination effect of the suprathermal populations of these species is heretofore unknown.

During energetic solar wind events, energetic electrons penetrate much deeper than suprathermal and energetic ions, so a dielectric potential difference may build up inside the surface up to a point of breakdown, when an electric arc would abruptly sublime or vaporize material along the arc path; however, we note that the efficiency and weathering effect of this dielectric breakdown process in various solar system environments is debated (e.g., Hapke, 2022; Jordan, 2022). Finally, several laboratory experiments have shown that suprathermal ions may alter the reflectance spectra of airless bodies at visible and infrared wavelengths (e.g., Brunetto & Strazzulla, 2005; Brunetto et al., 2014; Chrbolková et al., 2021; Lantz et al., 2015; Rubino et al., 2020).

One of the critical steps toward understanding the space weathering effects of precipitating ions lies in the characterization of the ion environment seen by the planetary surfaces, including the study of the intensity, anisotropy, and time variability of the ion fluxes depending on ion species, charge state, and energy. Some of the weathering effects listed above are short-term effects, for instance the sourcing of exospheres by ion sputtering which can be enhanced during the passage of an Interplanetary Coronal Mass Ejection (ICME) (Killen et al., 2012) or dielectric breakdown during solar energetic particle events. However, in this article, we focus on weathering effects that develop on time scales of hundreds to thousands of years and that can be caused by suprathermal ions: the creation of amorphous rims, modification of reflectance spectra, and contamination of elemental isotopic composition.

Previous work already characterized some long-term properties of the bombarding solar wind ions. At the Moon, Poppe et al. (2018) combined 5 years of ARTEMIS proton measurements to establish the long-term averaged environment encountered by the lunar surface. Based on this characterization, the previous authors proposed that the suprathermal protons and helium ions may be at the origin of the lunar amorphous rims that appear much thicker than the penetration depth of thermal ions. However, the ARTEMIS instrumentation has no ion mass resolution, so all observed ions were assumed to be protons.

To investigate the importance of the solar wind heavy ions for long-term space weathering of airless bodies, Nénon and Poppe (2020) compiled years of omnidirectional measurements (averaged over all directions of the sky) of light and heavy ions at thermal, suprathermal, and energetic energies by ACE, Wind, STEREO, ARTEMIS and MAVEN. They contrasted their long-term estimate of ion fluxes with the seminal work of Mewaldt et al. (2001) who presented one of the few available complete spectra of solar wind ions accumulated over a long

period of time. In their publication, Mewaldt et al. (2001) relied on 11 months of measurements accumulated in 1999 by the ACE-SWICS instrument for  $E_k < 100$  keV/q ions (thermal and suprathermal ions). For the more energetic suprathermal and energetic ions, Mewaldt et al. (2001) relied on 2.5 years of data from the ACE-ULEIS experiment from 1997 to 2000.

Figure 1 of Nénon and Poppe (2020) shows that the data sets publicly available at that time clearly confirm the omnidirectional spectra proposed by Mewaldt et al. (2001) for protons and helium ions in the suprathermal energy range. However, for ions heavier than helium like oxygen and iron, such validation was possible only in the energetic regime, so the thermal and suprathermal populations remained constrained only by the 11-month measurements accumulated by ACE-SWICS in 1999 and published by Mewaldt et al. (2001). Nevertheless, using the Mewaldt oxygen and iron spectra together with simulations of ion-matter interaction, Nénon and Poppe (2020) have shown that the suprathermal heavy ions of the solar wind may accelerate by up to 50% the development of the thick amorphous rims observed in lunar and asteroid samples. This conclusion is strongly dependent on the Mewaldt et al. (2001) fluxes of suprathermal heavy ions and deserves to be confirmed with a longer estimate of heavy ion fluxes.

Furthermore, the exact space weathering effects that develop in a specific location of an airless body surface depend on the bombardment pattern of the impacting ions, that is, the exact flux impacting each location. For instance, the thermal solar wind forms a beam of ions flowing parallel to the ecliptic plane in the lunar reference frame. Thermal solar wind ions therefore cannot access inside the Permanently Shadowed Regions (PSRs) of the lunar polar craters, unless an ambipolar electric field deflects their trajectory (e.g., Rhodes & Farrell, 2020; Zimmerman et al., 2011). The study of ion anisotropy and the characterization of out-of-ecliptic ion populations are therefore relevant to understanding the space weathering of lunar PSRs.

Regarding the study of out-of-ecliptic ion populations, Nénon and Poppe (2021) estimated the long-term-averaged anisotropy of the ion fluxes encountered by the Moon based on 8 years of ARTEMIS measurements. For ions with an energy per charge  $E_k < 30$  keV/q, they have shown that the northward and southward fluxes of ions that can directly enter lunar polar craters are dominated by ions encountered inside the terrestrial magnetosphere and not in the solar wind. However, this previous analysis could not study heavy ions (only protons) nor the contribution of suprathermal ions ( $E_k > 30$  keV/q).

In this article, we employ the recently released data set of suprathermal heavy ions observed by the Wind-SMS-STICS experiment (see Section 2) from 2004 to 2021 to confirm the findings of Nénon and Poppe (2020) regarding the role of ions heavier than helium for space weathering of planetary surfaces at depth. We also show that the Wind-SMS-STICS experiment enables us to compute the flux of suprathermal light and heavy ions that directly weather the interior of lunar polar craters when the Moon is exposed to the solar wind upstream of the terrestrial bow shock. The energy range covered by Wind-SMS-STICS also enables us to investigate at which energy suprathermal ion transition from a thermal beam to the quasi-isotropic distribution observed for energetic ions (e.g., Joyce et al., 2013).

The article is organized as follows: Section 2 presents the Wind-SMS-STICS instrumentation that we rely on to constrain the long-term averaged characteristics of the suprathermal ion fluxes bombarding the Moon. Section 3 then discusses a case study of enhanced suprathermal heavy ions during an ICME event. Section 4 presents the long-term averaged omnidirectional flux of the ions and contrast our results with previous estimates. Section 5 details our findings on the long-term anisotropy of suprathermal ions and presents the long-term flux of out-of-ecliptic suprathermal ions that weather lunar polar craters. Finally, our findings and their implications for space weathering are summarized and discussed in Section 6.

## 2. Methods: The Wind-SMS-STICS Experiment in Orbit Around L1 Since June 2004

### 2.1. Wind-STICS Observes the Full 3D Distribution of Suprathermal Ions in Double and Triple Coincidence

Wind was launched in 1994 and has remained in orbit around the Sun-Earth libration point L1 since June 2004. The Wind-SWICS/MASS/STICS (Wind-SMS, Gloeckler et al., 1995) package consists of three experiments designed to observe the thermal, suprathermal, and energetic ions of the solar wind and resolve their mass, charge state, kinetic energy, and anisotropy. In the SMS package, STICS (SupraThermal Ion Composition Spectrometer)

is a unique experiment tailored for the challenging observation of the suprathermal heavy ions of the solar wind. STICS combines an electrostatic analyzer (noted E/q selection hereafter) which selects ions with an energy per charge between 6 keV/q and 230 keV/q, a time-of-flight measurement (TOF) with no post acceleration, and the detection of residual energy deposited in a Solid State Detector (SSD). The start signal of the TOF measurement is initiated by the crossing of a thin carbon foil, while the stop signal comes from the secondary electrons generated by the ion impact on the SSD. The E/q selection and TOF measurement enable the resolution of both the energy per charge and mass per charge of the ions. This type of measurement is referred to as “double coincidence.” However, the various species of the multiply-charged heavy ions of the solar wind have similar m/q: He<sup>++</sup> has a mass per charge of 2 amu/q, O<sup>6-8+</sup> has a mass per charge of 2–2.7 amu/q, C<sup>4-6+</sup> a m/q of 2–3 amu/q, Mg<sup>7-10+</sup> a m/q of 2.4–3.4, and Fe<sup>7-14+</sup> a m/q of 4–8 amu/q, which is close to that of He<sup>+</sup> (4 amu/q). The measurement of the SSD residual energy is therefore used in addition to E/q and TOF to unambiguously resolve ion energy, mass, and charge with the “triple coincidence” observation mode. The low energy detection threshold of the STICS SSD is of around 35 keV (Figure A20 of Chotoo (1998)).

Wind-STICS uses three telescopes to separate the field of view of the electrostatic analyzer in three different ranges of elevation angles around the ecliptic plane. The telescope labeled “2” focuses on the ions with an elevation angle between  $-26.5^\circ$  and  $+26.5^\circ$ , with  $0^\circ$  pointing in the ecliptic plane. Telescopes 1 and 3 observe elevation angles of  $+26.5^\circ$  to  $+79.5^\circ$  and  $-26.5^\circ$  to  $-79.5^\circ$ , respectively. They therefore observe out-of-ecliptic ions traveling southward for telescope 1 and northward for telescope 3. In the azimuthal direction, each telescope has an azimuthal aperture of  $\sim 5^\circ$ . The azimuthal spin of the Wind spacecraft enables the three telescopes of STICS to observe 98% of the sky every Wind rotation period (around 3 s).

## 2.2. Organization of the Wind-STICS Measurements in Energy, Angular, Mass per Charge, and Mass Bins

The electrostatic analyzer of STICS steps through 32 voltages corresponding to 32 ranges of energy per charge logarithmically spaced between 6 keV/q and 230 keV/q. Each voltage is kept constant during two spins of the Wind spacecraft; hence, a full sweep of energy per charge is achieved every 3 min. Ion measurements are organized in 48 angular sectors, with 16 azimuthal bins covering each  $22.5^\circ$  and 3 elevation bins corresponding to the three telescopes of STICS. The 16 azimuthal bins are labeled from “0” to “15” with sector “9” pointing toward the Sun.

Ion counts are sorted by the STICS Data Processing Unit (DPU) into boxes of E/q, TOF, and residual energy. Each box is then assigned on the ground to a specific ion species and charge state, based on the observed distribution of counts in the m/q – m space and E/q-TOF tracks.

## 2.3. Calibration of the Wind-STICS Experiment and Uncertainties in the Observed Fluxes

Ion counts are converted to fluxes using the instrument response function presented by Chotoo (1998) (geometric factors, start, stop, and SSD pulse detection efficiencies, deadtime correction, energy passband). The instrument response function was estimated on the ground with a calibration campaign conducted at Goddard and at the University of Berne. In-flight comparison with lower energy and higher energy measurements have been conducted by Chotoo (1998) for protons and helium ions and led the previous author to divide the previously estimated geometric factor of the instrument by a factor of  $\sim 2$ . We note that there has been no in-flight calibration of the Wind-STICS measurements for ions heavier than helium. Section 4 will present a comparison of Wind-STICS oxygen measurements with higher-energy observations by ACE-ULEIS, which will represent a preliminary in-flight calibration for oxygen.

Double and triple coincidence measurements have the advantage of being almost unaffected by penetrating radiation. However, data in a given m/q – m box (or E/q, TOF, and SSD box) can suffer from spillover from neighboring boxes. Furthermore, double coincidence measurements of heavy ions can be contaminated by a fraction of the intense flux of light ions that experience energy and direction straggling when passing through the Start carbon foil. The two latter issues can be estimated with the not-standard Pulse Height Analysis data set (PHA) for which the entire information of all ion events (E/q, TOF, SSD energy) is downlinked to Earth, rather than just binned by the DPU.

STICS PHA data analysis are presented in Figures 2.8 and 3.1 of Chotoo (1998) and in Figure 5.9 of Gruesbeck (2013) for specific days. Furthermore, Figure 5.7 of Gruesbeck (2013) accumulates PHA data for the

entire year of 2004. The previous analyses reveal that light ion straggling is not a strong source of noise for heavy ion observations, unlike for lower energy double-coincidence systems like MAVEN-STATIC (e.g., Nénon et al., 2021). This may be linked to the fact that STICS observes very energetic light ions that barely suffer from straggling when crossing the carbon foil. The studies of Chotoo (1998) and Gruesbeck (2013) also indicate that the  $m - m/q$  boxes can be set to cleanly isolate the ion species and charge states.

#### 2.4. Wind-STICS Data Availability

An early version of the Wind-STICS data set was publicly available on CDAWeb (<https://cdaweb.gsfc.nasa.gov/>) until June 2022 and contained only the proton and helium ion fluxes observed in triple coincidence. Double coincidence measurements and data for other ion species remained unavailable until June 2022. On this date, the Wind-STICS instrument team released on CDAWeb a data set of calibrated and validated counts, fluxes, and distribution functions with the native integration time of 3 min for the entire Wind mission until the end of December 2021 (see Open Research section). Double coincidence fluxes are provided for  $H^+$ ,  $He^{++}$ ,  $He^+$ ,  $O^+$ , and  $O^{6+}$  ions. Triple coincidence fluxes are available for the five previous species, as well as for  $C^{5+}$  and  $Fe^{10+}$  ions. STICS can resolve other charge states of oxygen, carbon, and iron ions. However, the available data set focuses on the listed charge states because they are the most commonly used to investigate the origin and dynamics of suprathermal heavy ions.

### 3. Case Study: The Energy Spectrum and Anisotropy of the Solar Wind Suprathermal Ions During an ICME Event

Figure 1 presents energy-time spectrograms of the ion counts observed by Wind-STICS with double coincidence logic for  $He^{++}$  and  $O^{6+}$  ions. The selected time period corresponds to one of the two ICME events studied by Gruesbeck et al. (2015) who focused on the omnidirectional charge state of heavy ions observed by the ACE-SWICS (thermal ions) and Wind-STICS (suprathermal) experiments. Here, we expand on the Gruesbeck et al. (2015) study by investigating the energy spectra and anisotropy of the suprathermal ions during the event. We note that the Moon remained inside the terrestrial magnetosphere at the time period shown, so the studied ICME informs on conditions that the Moon could encounter, not on an event that actually weathered the lunar surface.

Panels a and c of Figure 1 show the counts observed by telescope 2 of STICS (ions flowing parallel to the ecliptic plane) labeled “T2” and summed over all azimuthal sectors, while panels b and d present Southward ions observed by telescope 1 (all azimuthal sectors). We find that telescope 3 observations (Northward ions) are similar to those of telescope 1. Ion counts are presented rather than ion fluxes to highlight the low level and sporadicity of the Wind-STICS counts, even during an ICME event. For kinetic energies lower than approximately 30 keV/nucleon, in-ecliptic ion fluxes (panels a and c) are much higher than the out-of-ecliptic component (panels b and d). One can see that the count levels for  $He^{++}$  ions at  $E_k > 30$  keV/nucleon seem similar for the in-ecliptic and out-of-ecliptic components (panels a and b). For high-energy  $O^{6+}$  ions, the extremely low level of counts integrated over less than 3 min does not enable a comparison of the in-ecliptic and out-of-ecliptic fluxes.

Panel e shows the in-ecliptic and out-of-ecliptic energy spectra of  $He^{++}$  and  $O^{6+}$  ions averaged over the entire 2-day period and observed in double and triple coincidence. Panel f details the total number of counts used and shows that most of the points of panel f rely on more than 10 counts, except for the challenging triple coincidence observation of out-of-ecliptic  $O^{6+}$  ions. For the latter observation, ion counts need to be integrated over a longer time period, as done in Section 4.

In panel e, the fluxes of  $>15$  keV/nucleon  $He^{++}$  ions observed in double coincidence (blue curves) are in agreement with those observed in triple coincidence (black curves), which tends to show that the instrumental response for  $He^{++}$  ions is correctly estimated. However,  $O^{6+}$  ion fluxes observed in double coincidence (red curves) are a factor of 3–5 higher than those in triple coincidence (magenta). The instrumental response for  $O^{6+}$  ion fluxes may therefore not be adequately estimated. Section 4 shows that this feature is also found in the long-term averaged fluxes.

We also find that at energies lower than 15 keV/nucleon (60 keV) and close to the SSD threshold of  $\sim 30$  keV, triple coincidence  $He^{++}$  fluxes (black curves) drop with decreasing energy. A similar feature is seen for  $<5$  keV/nucleon



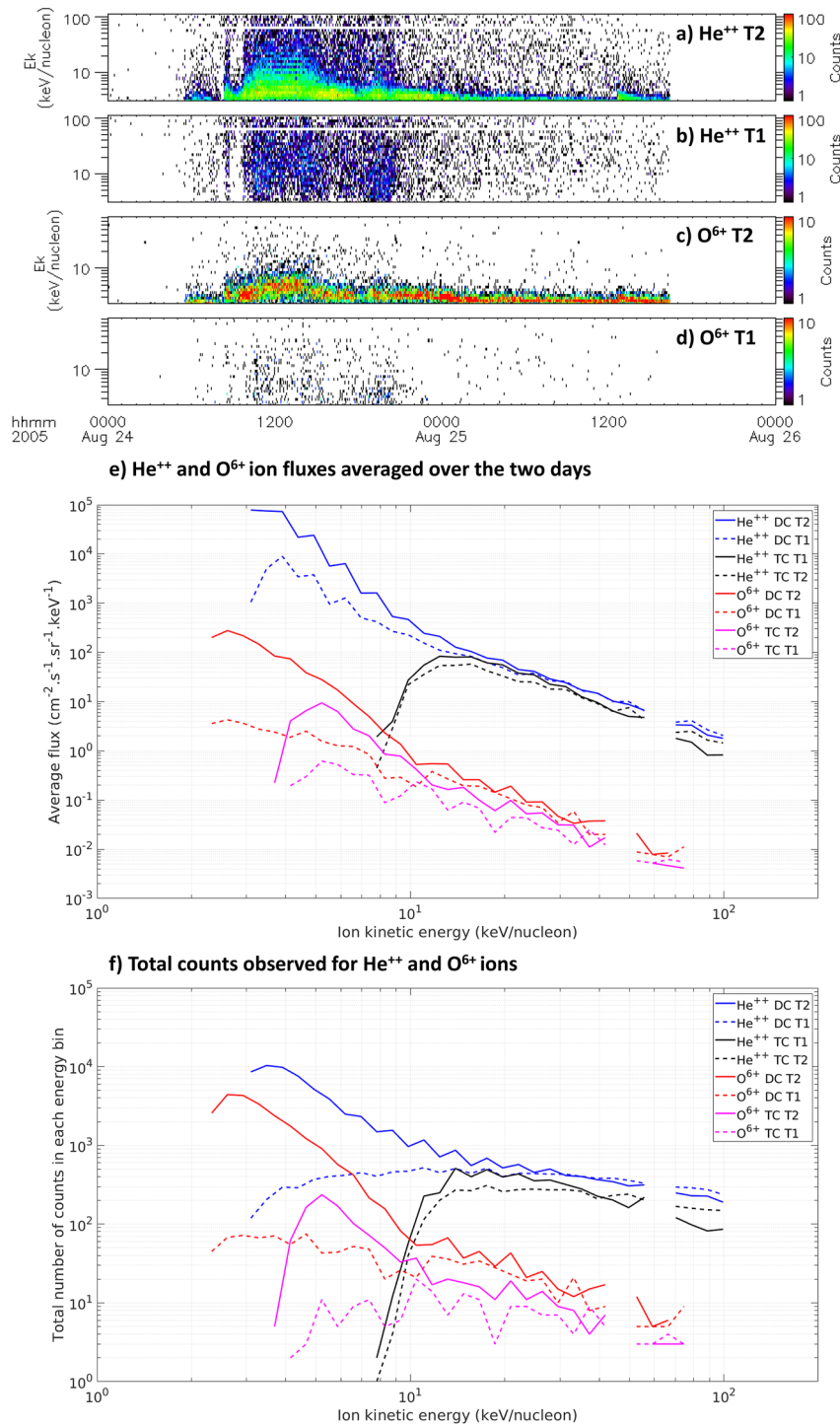


**Figure 1.** (a) Energy-time spectrogram of the He<sup>++</sup> ion counts observed by the in-ecliptic telescope 2 (labeled “T2”) of Wind-STICS in double coincidence with the native 3-min resolution. Ion counts are summed over all azimuthal sectors. (b) same as panel a but for the He<sup>++</sup> ion counts observed by the out-of-ecliptic telescope 1. (c) same as panel a but for O<sup>6+</sup> ions. (d) same as b but for O<sup>6+</sup> ions. (e) He<sup>++</sup> and O<sup>6+</sup> ion fluxes averaged over the 2-day period and observed in double and triple coincidence. (f) total number of counts corresponding to the fluxes of panel (e).

O<sup>6+</sup> ions (<80 keV) observed in triple coincidence (magenta curve). This may highlight that the SSD detection efficiency is overestimated for ions with a kinetic energy lower than ~60–80 keV, at least during this case study ICME event. Section 4 shows that this is a recurrent feature of the Wind-STICS observations.

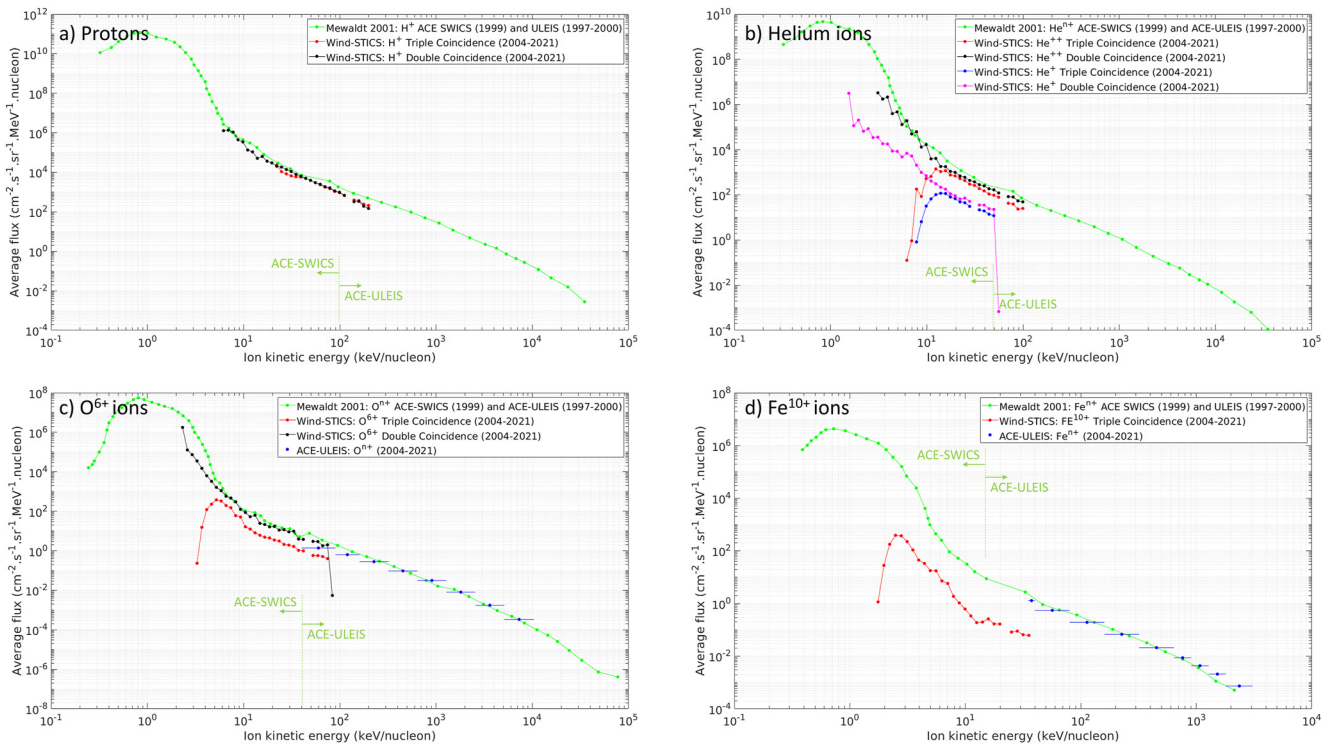


**Figure 2.** The long-term-averaged omnidirectional energy spectra of suprathermal ions observed by Wind-STICS and compared with the estimates published by Mewaldt et al. (2001). The vertical green line delimits the energy below which Mewaldt et al. (2001) relied on ACE-SWICS and above which they used ACE-ULEIS measurements.

The solid and dashed lines on panel e compare the energy spectra observed by the telescopes 2 (in-ecliptic) and 1 (out-of-ecliptic), respectively. They show that the flux of in-ecliptic ions is more than one order of magnitude higher than that of out-of-ecliptic ions at the lowest energies observed by STICS. However, in-ecliptic and out-of-ecliptic ion fluxes converge as ion energy increases. We therefore find that during this case study ICME event, the interior of lunar polar craters should be weathered by the same flux of  $>15$  keV/nucleon  $\text{He}^{++}$  and  $\text{O}^{6+}$  ions as anywhere else on the lunar surface. Section 5 shows that the isotropic nature of these high energy ions also appears in the long-term averaged fluxes.

#### 4. The Long-Term-Averaged Omnidirectional Flux of the Solar Wind Ions Observed by Wind-STICS

Figure 2 presents the omnidirectional spectrum of protons,  $\text{He}^{++}$ ,  $\text{He}^+$ ,  $\text{O}^{6+}$ , and  $\text{Fe}^{10+}$  ions observed by Wind-STICS and averaged over more than 17 years (June 2004–December 2021). Omnidirectional measurements combine the observations from all the telescopes in all the azimuthal sectors.

Figure S1 in Supporting Information S1 shows that the accumulation over such a long period of time provides a large number of counts at most energies and species with a therefore negligible counting statistics error. The green curves on Figure 2 give the spectra published by Mewaldt et al. (2001) who relied on 11 months of ACE-SWICS data for energies lower than the green vertical line, and on 2.5 years of ACE-ULEIS measurements above this energy. Mewaldt et al. (2001) present all ion charge states together (noted  $\text{A}^{n+}$  for specie A), while the Wind-STICS data presented here show only a few charge states.

For suprathermal protons and helium ions, double coincidence and triple coincidence fluxes (black, red, magenta, and blue curves on panels a and b) are in agreement, which tends to confirm that the instrumental response for protons and helium ions is correctly estimated, at least for energies greater than 70 keV. Below this energy, the decreasing flux of triple coincidence helium ions with decreasing energy indicates that the SSD sensitivity estimated by Chotoo (1998) may be overestimated for helium ions. The issue of falling fluxes close to the SSD

threshold is also seen in the triple coincidence spectra of oxygen (panel c) and iron ions (panel d). Overall, correcting ion fluxes close to the SSD threshold may be too challenging because of the small number of observed counts (Figure S1 in Supporting Information S1), so the reader may disregard triple coincidence helium, oxygen, and iron ion fluxes at energies lower than around 70 keV (or energy per nucleon lower than 15 keV/nucleon, 6 keV/nucleon, and 2.5 keV/nucleon, respectively). Proton measurements observed in triple coincidence do not exhibit the same issue, maybe because protons transfer their energy to the SSD more efficiently than heavies.

The 17-year averaged fluxes of protons and helium ions observed by Wind-STICS are in excellent agreement with the 11-month estimate of Mewaldt et al. (2001), both in the spectral shape and in absolute intensity. Nénon and Poppe (2020) reached the same conclusion with triple coincidence STICS measurements, but the double coincidence data, which was not available in 2020 (see Section 2.4), extends the previous conclusions to lower energies. We therefore confirm the space weathering conclusions of Nénon and Poppe (2020) that were based on the Mewaldt spectral estimates for protons and helium ions, including the fact that helium ions are likely responsible for most of the atomic displacements at depth greater than 40 nm in a typical regolith with a density of 3.8 g/cc.

We can now also study the importance of suprathermal singly charged  $\text{He}^+$  ions (Figure 2b) for airless body space weathering. These ions are likely ionization products of interstellar neutral helium (e.g., Gloeckler & Geiss, 1998). At 1 AU, we find with Wind-STICS that the long-term flux of suprathermal  $\text{He}^+$  is negligible compared to the flux of solar wind  $\text{He}^{++}$  (Figure 2b). We however note that even if suprathermal  $\text{He}^+$  ion fluxes are negligible over those of  $\text{He}^{++}$ , the singly charged helium may still alter the isotopic composition of airless body surfaces if  $\text{He}^+$  ions have a different isotopic ratio (e.g.,  $^3\text{He}/^4\text{He}$ ) than  $\text{He}^{++}$ , which cannot be resolved with the STICS instrumentation.

For suprathermal  $\text{O}^{6+}$  ions, the double-coincidence fluxes (black curve on panel c) are a factor of 3–5 higher than triple coincidence (red curve), unlike protons and helium ions for which double and triple coincidence agree between each other. We therefore find in the long-term averaged spectrum of oxygen the same issue as in the case study presented in Section 3. Nevertheless, the spectral shapes of the  $\text{O}^{6+}$  ion fluxes observed in double and triple coincidences agree not only between each other but also with the spectrum reported by Mewaldt et al. (2001) (green curve). On Figure 2c, the blue dots show the long-term averaged flux of higher energy oxygen observed by ACE-ULEIS, computed from 2004 to 2021 with the MSSP2 tool (PI: John Cooper): [https://omniweb.gsfc.nasa.gov/ftpbrowser/flux\\_spectr\\_m2.html](https://omniweb.gsfc.nasa.gov/ftpbrowser/flux_spectr_m2.html).

As the ACE-ULEIS fluxes are consistent with the Mewaldt estimate at high energy and given that the spectral slope of  $\text{O}^{6+}$  ions observed by Wind-STICS is in relative agreement with the Mewaldt results, we can conclude that the recently released 17-year data set of  $\text{O}^{6+}$  ions observed using STICS confirms the long-term spectra of  $\text{O}^{n+}$  published by Mewaldt et al. (2001) in the suprathermal energy range. This conclusion is relatively independent of the absolute calibration of the Wind-STICS oxygen fluxes. It relies on both the double and triple coincidence fluxes, so it is unaffected by possible contamination of double coincidence oxygen by other species.

The double coincidence flux of  $\text{O}^{6+}$  ions is in a remarkable absolute agreement with the Mewaldt flux and with ACE-ULEIS. This feature may show that the conversion of STICS counts to fluxes for double coincidence  $\text{O}^{6+}$  ions is correct *and* that a charge state of 6 would be the dominant charge state of suprathermal oxygen ions *and* that double coincidence  $\text{O}^{6+}$  ion fluxes are not contaminated by other ion species. However, if the double coincidence measurements tend to overestimate  $\text{O}^{6+}$  ion fluxes or if the real flux of  $\text{O}^{6+}$  ions is better estimated with triple coincidence (meaning the real flux of  $\text{O}^{6+}$  ions would be lower than the double coincidence one because of instrument calibration or because of contamination by other species), then the apparent agreement between double coincidence  $\text{O}^{6+}$  flux and ACE-ULEIS would in fact indicate that other oxygen charge states significantly contribute to the total oxygen flux. STICS observations for other oxygen charge states are not publicly available (see Section 2.4). However, Gruesbeck et al. (2015) have shown that the average charge state of suprathermal oxygen observed by STICS during two ICME events was of around 6.2 during one event and 6.0 during the other. It is therefore possible that the charge state of 6 is the dominant one over long periods of time for suprathermal oxygen ions. Wind-STICS therefore provides several strong lines of evidence that the Mewaldt estimate of long-term oxygen ion fluxes is representative of the longer-term fluence seen by airless body surfaces.

Finally, Figure 2d presents the long-term flux of  $\text{Fe}^{10+}$  ions observed by Wind-STICS in triple coincidence. If the absolute calibration of the  $\text{Fe}^{10+}$  ion fluxes is correct, one can estimate that the 10+ charge state would comprise



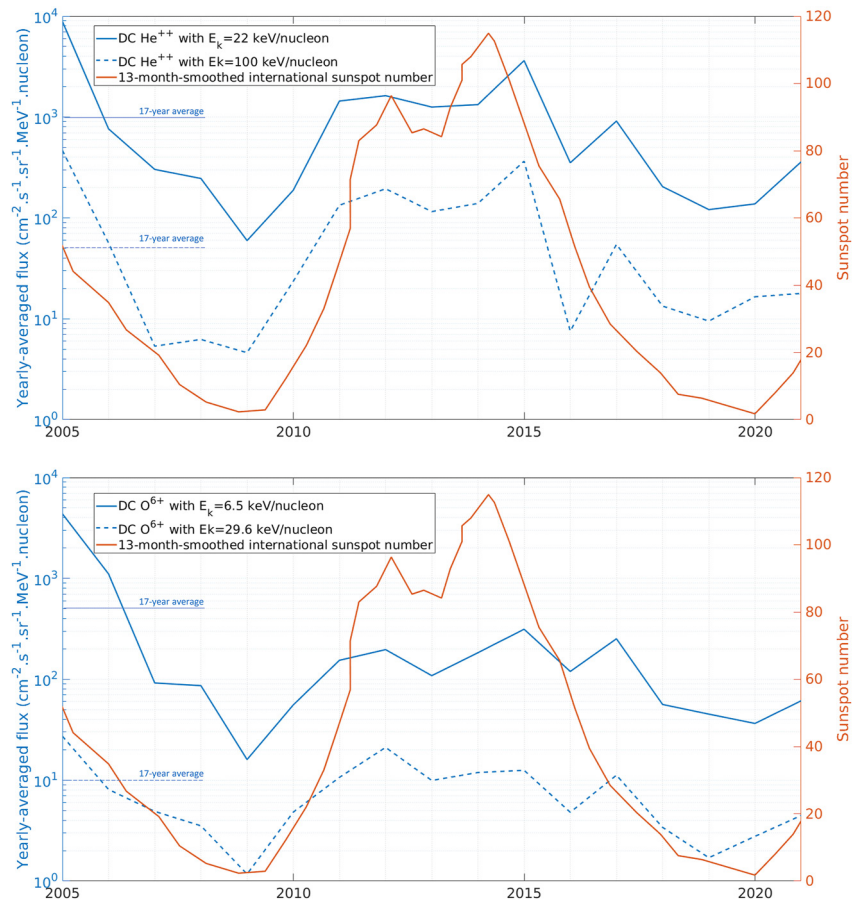


**Figure 3.** The time variability of yearly-averaged fluxes of He<sup>++</sup> ions (top panel) and O<sup>6+</sup> ions (bottom panel) observed by Wind-STICS in double coincidence, together with the 13-month smoothed international sunspot number. The horizontal solid and dashed lines on the left in the presence of the 17-year average fluxes for the two shown kinetic energies.

around 2%–4% of the total iron flux at suprathermal energies, which would be consistent with the charge distribution at thermal energy (noting that 10+ is the dominant charge state at thermal energy) (von Steiger et al., 2000; also Figure 2.2 of Gruesbeck (2013)).

Figure 3 presents yearly-averaged fluxes of He<sup>++</sup> ions and O<sup>6+</sup> ions observed by STICS in double coincidence at two energies per species chosen to be representative of the time variability observed for all kinetic energies. The 13-month smoothed international sunspot number retrieved at <https://www.sidc.be/SILSO/datafiles> is also presented and used as a proxy for solar activity. It shows that the yearly-averaged fluxes of suprathermal heavy ions vary by approximately two orders of magnitude over time. This variability seems to be correlated with solar activity (sunspot number). We note that the computation of the linear average of a quantity that greatly varies is biased toward high values, as shown with the horizontal lines of Figure 3. We also note that the 11-month estimate of Mewaldt et al. (2001) was conducted in 1999 near the solar maximum. The agreement between the 17-year-averaged fluxes of STICS and the Mewaldt estimates may therefore come from the lucky coincidence that (a) the long-term average of STICS is biased toward high values because the fluxes greatly change over time, and (b) the Mewaldt estimate is also biased toward high values because it was conducted near the solar maximum.

### 5. Anisotropy of the Solar Wind Ions Observed by Wind-STICS and the Flux of Suprathermal Ions Inside Lunar Polar Craters

Wind-STICS observes 98% of the full 3D ion distribution thanks to the spacecraft azimuthal spin and the three STICS telescopes. Telescope 2 is mounted to observe ions with a low elevation angle around the ecliptic plane (elevation angles of  $-26^\circ$  to  $+26^\circ$ ), while the telescopes 1 and 3 observe southward ions (pointing to elevation angle of  $+26^\circ$  to  $+79.5^\circ$ ) and northward ions ( $-26^\circ$  to  $-79.5^\circ$ ), respectively.

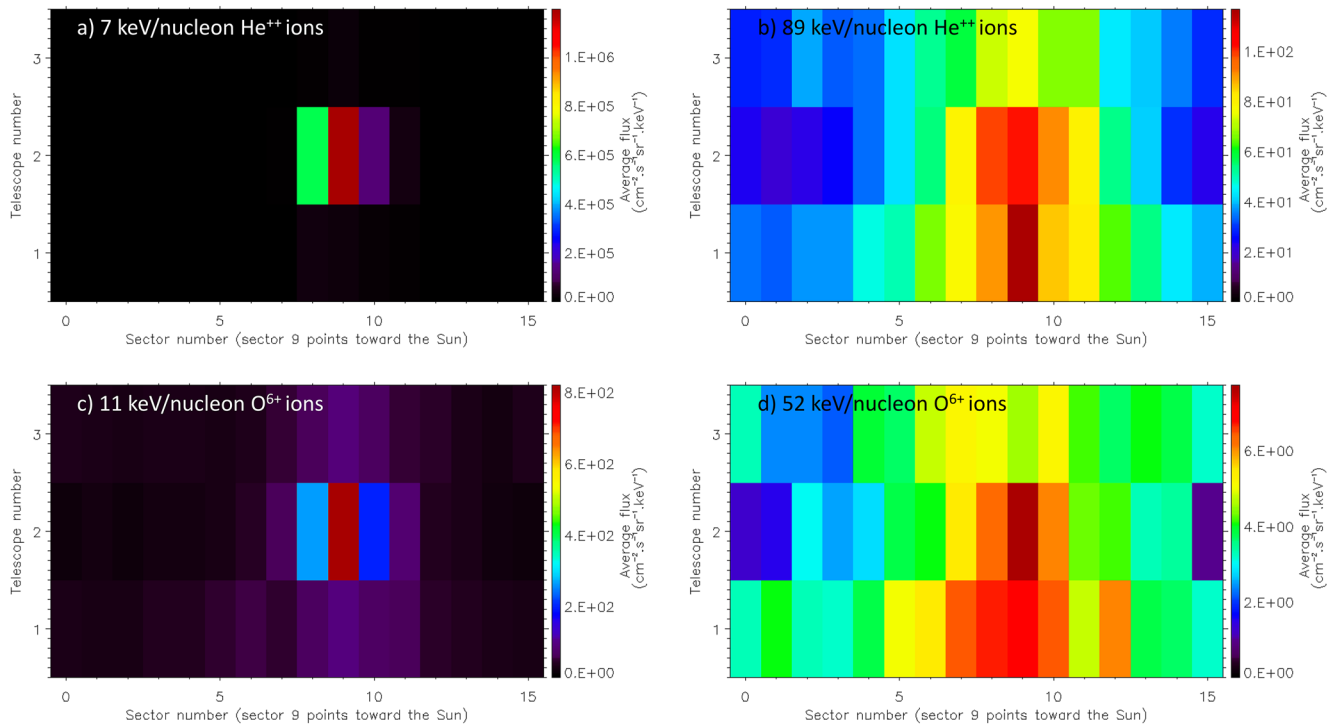


**Figure 4.** Anisotropy maps of the long-term-averaged fluxes of suprathermal ions observed by Wind-STICS in double coincidence as a function of elevation (telescope number on the y axis) and azimuthal sector (x axis).

The ions observed by telescope 3 with an elevation angle of  $26\text{--}79.5^\circ$  have direct access to the interiors of most of the South Pole craters (e.g., Haworth, Shoemaker, Faustini), including crater regions locally shielded from the horizontal solar wind (Rhodes & Farrell, 2020). The only exception may be the central floor of the South Pole crater named “Shackleton,” which is exposed to all ions with an elevation angle greater than  $35^\circ$ , while the telescope 3 observations may be dominated by  $26\text{--}35^\circ$  ions that would not reach the center of the crater. Nevertheless, we show in Section 6 that the Wind-STICS telescope 3 observations likely inform the flux of ions weathering the center of Shackleton, and therefore all lunar PSRs. The anisotropy of ions is studied hereafter in the Wind spacecraft reference frame which is equivalent to the reference frame of the Moon. Specifically, we do not convert ion anisotropies to the bulk plasma frame.

Figure 4 presents anisotropy maps of the long-term averaged flux (color bar) seen by the three telescopes of Wind-STICS (y axis) in the 16 azimuthal sectors (x axis), with sector 9 pointing toward the Sun. Anisotropy maps for other species and all STICS energies are available in an online repository (link in the acknowledgments section).

Close to the lowest energies observed by STICS in double coincidence (Figure 4, panels a and c), the ion flux seen by the out-of-ecliptic telescopes (1 and 3) is negligible over the in-ecliptic flux (telescope 2) and is not fully visible with the linear scale of Figure 4. At high energy (panels b and d), the intensity of out-of-ecliptic ion fluxes becomes comparable to that of antisunward fluxes. A slight excess of a factor of 2 for ion fluxes in the antisunward direction (sector 9) remains.

Figure 5 further quantifies the long-term flux anisotropy of protons,  $\text{He}^{++}$ ,  $\text{O}^{6+}$ , and  $\text{Fe}^{10+}$  ions observed by Wind-STICS. The black curves present the ion flux that impacts the equatorial subsolar point of the Moon and is integrated over a solid angle of  $2\pi$  sr around the Sun direction (i.e., taking into account the three telescopes in sectors 5 to 12). The magenta and red curves isolate the flux of ions that can directly weather inside most lunar polar craters by integrating the fluxes observed by the out-of-ecliptic telescopes 1 and 3 over all azimuthal sectors (corresponding to a solid angle of 4.4 sr). In particular, the red curve fluxes observed by telescope 3 directly bombard the interior of most South Pole craters. Figure S2 in Supporting Information S1 gives the total number of counts behind the fluxes of Figure 5.

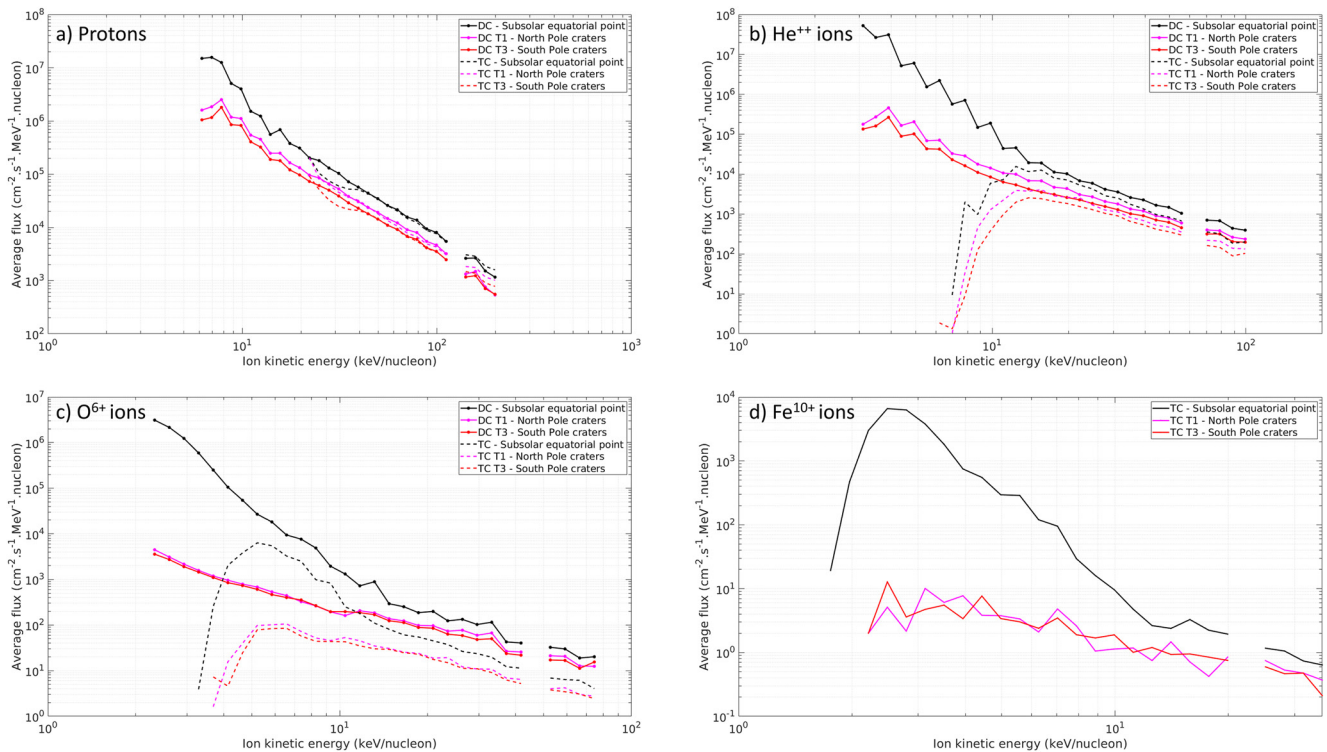


**Figure 5.** The averaged flux of suprathermal ions that impact the subsolar point (integrated over  $2\pi$  sr) or that directly enter inside the lunar polar craters (integrated over 4.4 sr) is observed in double coincidence (labeled “DC”) or in triple coincidence (“TC”). “T1” and “T3” refer to the telescopes 1 and 3 of Wind-STICS, respectively.

For kinetic energies lower than around 15 keV/nucleon, the subsolar flux is orders of magnitude larger than the Northward and Southward fluxes. However, for energies higher than 15 keV/nucleon, the subsolar and polar fluxes converge (i.e., with a flux difference lower than a factor of 2), likely because of the increasing gyroradius of the suprathermal ions. Wind-STICS therefore reveals that most of the interiors of lunar polar craters are weathered by at least the same flux of  $>15$  keV/nucleon ions as anywhere else on the lunar surface. While the number flux of these ions is negligible compared to the flux of thermal ions, their larger energies enable them to affect lunar grains or ice at depths much larger than thermal ions.

## 6. Summary and Discussion

The Wind-SMS-STICS experiment has observed for more than 17 years the full 3D distribution of the suprathermal light and heavy ions of the solar wind with energy, mass, charge, and angular resolution. This unprecedented data set offers us the capability to estimate the long-term averaged flux of these ions in order to pave the way for understanding the space weathering effects they may have on airless body surfaces, including that of the Moon. While the total flux of suprathermal ions is negligible compared to that of thermal ions, their larger kinetic energy enables such suprathermal ions to penetrate and alter planetary surfaces deeper than the thermal population. Possible space weathering effects associated with suprathermal ions include (a) the creation of amorphous rims thicker than the penetration depth of thermal ions, (b) the modification of optical reflectance at wavelengths sensitive to the penetration depth of suprathermal ions (typically  $>100$  nm), including infrared, and (c) the exogenous contamination of planetary samples at depth.

Previously, Poppe et al. (2018) and Nénon and Poppe (2020) investigated the importance of the solar wind suprathermal light and heavy ions for space weathering based on years of ion measurements collected by several spacecraft, and numerical simulations of ion-matter interactions. However, the long-term flux of ions heavier than protons in the suprathermal energy range of around 10 keV/nucleon to 100 keV/nucleon was poorly constrained due to the lack of publicly available data. Nénon and Poppe (2020) therefore relied on the long-term averaged fluxes published by Mewaldt et al. (2001) based on only 11 months of measurements.

In this article, we take advantage of the 17-year Wind-SMS-STICS data set to constrain the long-term energy spectrum and anisotropy of suprathermal  $H^+$ ,  $He^{++}$ ,  $He^+$ ,  $O^{6+}$ , and  $Fe^{10+}$  ions. Our investigation reveals that future work may revisit the absolute calibration of the STICS triple coincidence systems for ions heavier than helium because the triple coincidence fluxes of  $O^{6+}$  ions are a factor of 3–5 lower than not only the STICS double coincidence fluxes, but also of the higher-energy observations of ACE-ULEIS. A new estimate of the triple coincidence response function may also improve the absolute calibration of other ion species and charge states that are not resolved in double coincidence, such as  $Fe^{10+}$ .

Nevertheless, the measurements of Wind-STICS confirm that the omnidirectional energy spectra published by Mewaldt et al. (2001) for protons, helium, and oxygen ions are representative of the long-term ion fluxes that weather airless body surfaces at 1 AU. This agreement may come from the lucky coincidence that the Mewaldt estimate was conducted near the solar maximum, while the 17-year STICS average is biased toward high flux values (see Figure 3 and Section 4).

The agreement between the long-term flux estimates of STICS and Mewaldt tends to validate the two main space weathering conclusions drawn by Nénon and Poppe (2020). Firstly, suprathermal ions with a kinetic energy greater than a few keV/nucleon contribute to less than 1% to ion sputtering (see Figure 2b of Nénon and Poppe (2020)). Secondly, the heavy ‘minor’ ions of the solar wind likely contribute to more than 20%–50% of atomic displacements at depth greater than 100 nm (assuming a 3.8 g/cc olivine), where they can therefore accelerate the development of amorphous rims and may alter the optical reflectance and composition of the material. Future work may attempt to convolve the long-term fluxes presented here with laboratory estimates of implantation rate, defect generation, and radiolysis effects of heavy ions on lunar rocks and ice, as done at the outer planet icy moons for instance (e.g., Cooper et al., 2001; Teolis et al., 2017).

The long-term-averaged anisotropy of suprathermal light and heavy ions is investigated for the first time thanks to the Wind-SMS-STICS data set, with the motivation to constrain the out-of-ecliptic ion fluxes that directly bombard the PSRs of the lunar polar craters. For the lowest energies observed by STICS, we find that the out-of-ecliptic flux is two to three orders of magnitude lower than the flux impacting the lunar dayside equator. However, for energies larger than 15 keV/nucleon, suprathermal ion fluxes become more and more isotropic, likely due to the increasing ion gyroradius. Figure 5 shows that most of the lunar polar crater interiors are weathered by the same flux of >15 keV/nucleon ions as anywhere else on the Moon.

The only lunar PSR region for which we cannot firmly constrain the precipitating ion flux is the central floor of Shackleton's crater because it is exposed to all ions with an elevation angle greater than  $35^\circ$ , while the STICS telescope observe  $26$ – $79.5^\circ$  ions and its signal may be dominated by  $26$ – $35^\circ$  ions. Still, the  $>26^\circ$  ions observed using STICS can reach the floor of Shackleton in all regions located more than 3 km from the center of the crater. Rhodes and Farrell (2020) have shown that these regions are largely protected from electrostatically-deflected thermal solar wind ions. We also note that the anisotropy maps provided in Figure 4 and in Supporting Information S1 indicate that suprathermal ion fluxes may become quasi-isotropic with increasing kinetic energy (according to the coarse elevation resolution of STICS). It is therefore likely that the STICS observation of  $26$ – $79^\circ$  ions also informs on the flux of  $>35^\circ$  ions that directly bombard the center of Shackleton. We conclude that most of the lunar polar craters, including most of the floor of Shackleton, are weathered by the same flux of >15 keV/nucleon ions as anywhere else on the lunar surface. This conclusion is also likely true for the center of Shackleton. The ion fluxes presented in Figure 5 therefore represent a first step toward understanding ion weathering in the lunar PSRs.

In this article, the long-term bombardment pattern of ions on the surface of the Moon has been discussed by assuming a totally unmagnetized Moon. However, the lunar crustal fields can locally deflect solar wind ions (Halekas et al., 2011; Lue et al., 2011; Saito et al., 2012). Furthermore, Poppe et al. (2021) have shown that the possible paleomagnetosphere of the Moon could have fractionated in the past the solar wind ion bombardment in a non-linear fashion depending on ion mass and charge state. This previous work considered only the thermal ion population, so future work may investigate the effect of a lunar paleomagnetosphere on suprathermal ion precipitation.



## Data Availability Statement

The 3-min counts and fluxes observed by Wind-STICS and used in this article are publicly available on CDAWeb (<https://cdaweb.gsfc.nasa.gov/>) in the “WI\_L2-3MIN\_SMS-STICS-VDF-SOLARWIND” repository (Lepri, 2022). The numerical values of the fluxes shown in the figures and supplementary spectra and anisotropy maps are provided in the online repository of Nénon et al. (2023).

## Acknowledgments

TQ. N. acknowledges the support of CNES to the Lunar Gateway (order 4500072977), MMX, and Wind missions. A. R. P. acknowledges support from the NASA SSERVI LEADER team, Grant 80NSSC20M0060.

## References

- Brunetto, R., Lantz, C., Ledu, D., Baklouti, D., Barucci, M. A., Beck, P., et al. (2014). Ion irradiation of Allende meteorite probed by visible, IR, and Raman spectroscopies. *Icarus*, 237, 278–292. <https://doi.org/10.1016/j.icarus.2014.04.047>
- Brunetto, R., & Strazzulla, G. (2005). Elastic collisions in ion irradiation experiments: A mechanism for space weathering of silicates. *Icarus*, 179(1), 265–273. <https://doi.org/10.1016/j.icarus.2005.07.001>
- Chotoo, K. (1998). *Measurements of H<sup>+</sup>, He<sup>2+</sup>, and He<sup>+</sup> in corotating interacting regions at 1 AU* (PhD thesis). University of Maryland. Retrieved from [https://wind.nasa.gov/docs/SMS\\_ChotooThesis.pdf](https://wind.nasa.gov/docs/SMS_ChotooThesis.pdf)
- Chrbolková, K., Brunetto, R., Ďurech, J., Kohout, T., Mizohata, K., Malý, P., et al. (2021). Comparison of space weathering spectral changes induced by solar wind and micrometeoroid impacts using ion- and femtosecond-laser-irradiated olivine and pyroxene. *Astronomy & Astrophysics*, 654, A143. <https://doi.org/10.1051/0004-6361/202140372>
- Cooper, J. F., Johnson, R. E., Mauk, B. H., Garrett, H. B., & Gehrels, N. (2001). Energetic ion and electron irradiation of the icy Galilean satellites. *Icarus*, 149(1), 133–159. <https://doi.org/10.1006/icar.2000.6498>
- Gloeckler, G., Balsiger, H., Bürgi, A., Bochsler, P., Fisk, L. A., Galvin, A. B., et al. (1995). The solar wind and suprathermal ion composition investigation on the WIND spacecraft. *Space Science Reviews*, 71(1–4), 79–124. <https://doi.org/10.1007/bf00751327>
- Gloeckler, G., & Geiss, J. (1998). Interstellar and inner source pickup ions observed with SWICS on Ulysses. *Space Science Reviews*, 86(1–4), 127–159. <https://doi.org/10.1023/a:1005019628054>
- Gruesbeck, J. R. (2013). *Exploring the origin of coronal mass ejection plasma from in-situ observations of ionic charge state distribution* (PhD thesis). University of Michigan. Retrieved from [https://wind.nasa.gov/docs/Gruesbeck\\_2013PhDThesis.pdf](https://wind.nasa.gov/docs/Gruesbeck_2013PhDThesis.pdf)
- Gruesbeck, J. R., Lepri, S. T., Zurbuchen, T. H., & Christian, E. R. (2015). Evidence for local acceleration of suprathermal heavy ion observations during interplanetary coronal mass ejections. *The Astrophysical Journal*, 799(1), 57. <https://doi.org/10.1088/0004-637x/799/1/57>
- Halekas, J. S., Saito, Y., Delory, G. T., & Farrell, W. M. (2011). New views of the lunar plasma environment. *Planetary and Space Science*, 59(14), 1681–1694. <https://doi.org/10.1016/j.pss.2010.08.011>
- Hapke, B. (2022). Do deep electrical discharges initiated by solar energetic particle events occur in the lunar regolith? *Icarus*, 372, 114758. <https://doi.org/10.1016/j.icarus.2021.114758>
- Jordan, A. P. (2022). Reevaluating how charged particles cause space weathering on airless bodies. *Icarus*, 376, 114878. <https://doi.org/10.1016/j.icarus.2021.114878>
- Joyce, C. J., Schwadron, N. A., Wilson, J. K., Spence, H. E., Kasper, J. C., Golightly, M., et al. (2013). Validation of PREDICCS using LRO/CRA TER observations during three major solar events in 2012. *Space Weather*, 11(6), 350–360. <https://doi.org/10.1002/swe.20059>
- Keller, L. P., Berger, E. L., Zhang, S., & Christoffersen, R. (2021). Solar energetic particle tracks in lunar samples: A transmission electron microscope calibration and implications for lunar space weathering. *Meteoritics & Planetary Science*, 56(9), 1685–1707. <https://doi.org/10.1111/maps.13732>
- Keller, L. P., & Zhang, S. (2015). Rates of space weathering in lunar soils. In *Space weathering of airless bodies: An integration of remote sensing data, laboratory experiments and sample analysis workshop* (p. 2056). LPI Contribution No. 1878.
- Killen, R. M., Hurley, D. M., & Farrell, W. M. (2012). The effect on the lunar exosphere of a coronal mass ejection passage. *Journal of Geophysical Research*, 117(E10), E00K02. <https://doi.org/10.1029/2011je004011>
- Lantz, C., Brunetto, R., Barucci, M. A., Dartois, E., Duprat, J., Engrand, C., et al. (2015). Ion irradiation of the Murchison meteorite: Visible to mid-infrared spectroscopic results. *Astronomy & Astrophysics*, 577, A41. <https://doi.org/10.1051/0004-6361/201425398>
- Lepri, S. T. (2022). WI\_L2-3MIN\_SMS-STICS-VDF-SOLARWIND [Dataset]. NASA Space Physics Data Facility, Coordinated Data Analysis Web. Retrieved from <https://cdaweb.gsfc.nasa.gov/>
- Lue, C., Futaana, Y., Barabash, S., Wieser, M., Holmström, M., Bhardwaj, A., et al. (2011). Strong influence of lunar crustal fields on the solar wind flow. *Geophysical Research Letters*, 38(3), L03202. <https://doi.org/10.1029/2010gl046215>
- Mewaldt, R. A., Cohen, C. M. S., Mason, G. M., Haggerty, D. K., & Desai, M. I. (2007). Long-term fluences of solar energetic particles from H to Fe. *The Composition of Matter*, 323–328. [https://doi.org/10.1007/978-0-387-74184-0\\_32](https://doi.org/10.1007/978-0-387-74184-0_32)
- Mewaldt, R. A., Mason, G. M., Gloeckler, G., Christian, E. R., Cohen, C. M. S., Cummings, A. C., & Zurbuchen, T. H. (2001). Long-term fluences of energetic particles in the heliosphere. In *AIP Conference Proceedings* (Vol. 598, No. 1, pp. 165–170). American Institute of Physics. <https://doi.org/10.1063/1.1433995>
- Nénon, Q., & Poppe, A. R. (2020). On the long-term weathering of airless body surfaces by the heavy minor ions of the solar wind: Inputs from ion observations and SRIM simulations. *The Planetary Science Journal*, 1(3), 69. <https://doi.org/10.3847/psj/abbe0c>
- Nénon, Q., & Poppe, A. R. (2021). Bombardment of lunar polar crater interiors by out-of-ecliptic ions: ARTEMIS observations. *The Planetary Science Journal*, 2(3), 116. <https://doi.org/10.3847/psj/abfda2>
- Nénon, Q., Poppe, A. R., Rahmati, A., & McFadden, J. P. (2021). Implantation of Martian atmospheric ions within the regolith of Phobos. *Nature Geoscience*, 14(2), 61–66. <https://doi.org/10.1038/s41561-020-00682-0>
- Nénon, Q., Raines, J. M., & Poppe, A. R. (2023). The long-term flux of the solar wind suprathermal ions that precipitate on the lunar surface [Dataset]. Figshare <https://doi.org/10.6084/m9.figshare.24156726>
- Pieters, C. M., & Noble, S. K. (2016). Space weathering on airless bodies. *Journal of Geophysical Research: Planets*, 121(10), 1865–1884. <https://doi.org/10.1002/2016je005128>
- Poppe, A. R., Farrell, W. M., & Halekas, J. S. (2018). Formation timescales of amorphous rims on lunar grains derived from ARTEMIS observations. *Journal of Geophysical Research: Planets*, 123(1), 37–46. <https://doi.org/10.1002/2017je005426>
- Poppe, A. R., Garrick-Bethell, I., & Fatemi, S. (2021). Fractionation of solar wind minor ion precipitation by the lunar paleomagnetosphere. *The Planetary Science Journal*, 2(2), 60. <https://doi.org/10.3847/psj/abea7d>
- Rhodes, D. J., & Farrell, W. M. (2020). Mapping the predicted solar wind hydrogen flux in lunar south pole craters. *The Planetary Science Journal*, 1(1), 13. <https://doi.org/10.3847/psj/ab8939>

- Rubino, S., Lantz, C., Baklouti, D., Leroux, H., Borondics, F., & Brunetto, R. (2020). Space weathering affects the remote near-IR identification of phyllosilicates. *The Planetary Science Journal*, *1*(3), 61. <https://doi.org/10.3847/psj/abb94c>
- Saito, Y., Nishino, M. N., Fujimoto, M., Yamamoto, T., Yokota, S., Tsunakawa, H., et al. (2012). Simultaneous observation of the electron acceleration and ion deceleration over lunar magnetic anomalies. *Earth Planets and Space*, *64*(2), 83–92. <https://doi.org/10.5047/eps.2011.07.011>
- Schaible, M. J., Dukes, C. A., Hutcherson, A. C., Lee, P., Collier, M. R., & Johnson, R. E. (2017). Solar wind sputtering rates of small bodies and ion mass spectrometry detection of secondary ions. *Journal of Geophysical Research: Planets*, *122*(10), 1968–1983. <https://doi.org/10.1002/2017je005359>
- Teolis, B. D., Plainaki, C., Cassidy, T. A., & Raut, U. (2017). Water ice radiolytic O<sub>2</sub>, H<sub>2</sub>, and H<sub>2</sub>O<sub>2</sub> yields for any projectile species, energy, or temperature: A model for icy astrophysical bodies. *Journal of Geophysical Research: Planets*, *122*(10), 1996–2012. <https://doi.org/10.1002/2017je005285>
- Von Steiger, R., Schwadron, N. A., Fisk, L. A., Geiss, J., Gloeckler, G., Hefti, S., et al. (2000). Composition of quasi-stationary solar wind flows from Ulysses/Solar Wind Ion Composition Spectrometer. *Journal of Geophysical Research*, *105*(A12), 27217–27238. <https://doi.org/10.1029/1999ja000358>
- Wieler, R. (2016). Do lunar and meteoritic archives record temporal variations in the composition of solar wind noble gases and nitrogen? A reassessment in the light of Genesis data. *Geochemistry*, *76*(4), 463–480. <https://doi.org/10.1016/j.chemer.2016.06.001>
- Zimmerman, M. I., Farrell, W. M., Stubbs, T. J., Halekas, J. S., & Jackson, T. L. (2011). Solar wind access to lunar polar craters: Feedback between surface charging and plasma expansion. *Geophysical Research Letters*, *38*(19), L19202. <https://doi.org/10.1029/2011gl048880>